International Journal of Thermophysics manuscript No.
(will be inserted by the editor)

A Helmholtz Energy Equation of State for 3,3,3-Trifluoroprop-1-ene (R-1243zf)

Ryo Akasaka · Eric W. Lemmon

Received: date / Accepted: date

Keywords Density · Equation of state · Heat capacity · R-1243zf · Sound speed · Vapor pressure · Virial coefficient

Abstract A new fundamental equation of state expressed as a function of the Helmholtz energy is presented for 3,3,3-trifluoroprop-1-ene (R-1243zf). The

Ryo Akasaka

Department of Mechanical Engineering, Faculty of Science and Engineering, Kyushu Sangyo University, Fukuoka 8138503, Japan

Research Center for Next Generation Refrigerant Properties (NEXT-RP), International Institute for Carbon-Neutral Energy Research (WPI-I2CNER), Kyushu University, Fukuoka 8190395, Japan

E-mail: ryo-a@ip.kyusan-u.ac.jp

ORCID: 0000-0003-2641-6031

Eric W. Lemmon

Applied Chemicals and Materials Division, National Institute of Standards and Technology, Boulder, CO 80305, USA

E-mail: eric.lemmon@nist.gov

ORCID: 0000-0002-0974-0203

equation is valid from the triple point temperature (122.35 K) to 430 K at pressures up to 35 MPa. The expected uncertainties ($k = 2$) in calculated properties from the equation of state are 0.1 % for vapor pressures, 0.1 % for liquid densities, 1 % for vapor densities, 0.3 % for saturated liquid densities, 1 % for saturated vapor densities, 0.06 % for vapor-phase sound speeds, and 2 % for liquid-phase isobaric heat capacities. Differences between experimental and calculated vapor pressures are within 2 kPa in most cases. Uncertainties for caloric properties are particularly improved from the former equations of state. Various plots of constant-property lines demonstrate that not only does the equation exhibit correct behavior over all temperatures and pressures within the range of validity, but also that it shows reasonable extrapolation behavior at extremely low and high temperatures, and at high pressures.

1 INTRODUCTION

The substance 3,3,3-trifluoroprop-1-ene (CAS 677-21-4), also known as R-1243zf, with the chemical formula $C_3H_3F_3$ and a molar mass of 96.05113 $g \cdot mol^{-1}$ is an unsaturated hydrofluorocarbon refrigerant with a low global-warming potential (GWP) and zero ozone-depletion potential (ODP). The molecular structure of R-1243zf is shown in Fig. 1. The 100yr-GWP and atmospheric lifetime of R-1243zf are 0.29 and 8.7 days [1]. Due to its flammability, the refrigeration industry considers R-1243zf a constituent of refrigerant mixtures rather than a single-component refrigerant. Experimental and/or theoretical analyses of thermophysical properties and the performance of refrigeration cycles

have been reported for mixtures of R-1243zf with pentafluoroethane (R-125), 1,1,1,2-tetrafluoroethane (R-134a), 1,1-difluoroethane (R-152a), 1,1,1,2,3,3,3-heptafluoropropane (R-227ea), 2,3,3,3-tetrafluoroprop-1-ene (R-1234yf), and carbon dioxide (R-744) [2–7].

The first fundamental equation of state for R-1243zf was presented by Akasaka [8] in 2016. The residual part of this equation consists of only polynomial and exponential terms, which were fitted to early experimental data for the vapor pressure and liquid and vapor densities located in a limited range of fluid states. Caloric data were not used in the fitting because they were unavailable at that time. Subsequently, the second equation was developed by Akasaka and Lemmon [9] in 2019. The equation includes Gaussian terms in the residual part. Although the equation is based on the same experimental datasets as those used for the first equation, the Gaussian terms yield more reasonable behavior in the extrapolated and two-phase regions.

This work presents the third equation of state, which employs recently published experimental data including caloric properties, in addition to those used for the former two equations. New features are introduced for the residual part of the third equation; they help reduce the number of terms, avoid the intercorrelation between terms, and further improve the extrapolation behavior.

The following sections discuss the fundamental constants and available experimental data for R-1243zf, the functional form of the equation of state, the outline of fitting techniques, and the statistical analyses of deviations between

experimental and calculated properties. Ancillary equations for the saturation properties are provided for rapid calculations. Demonstrative plots are given to show reasonable behavior of the equation in the critical and extrapolated regions. Finally, expected uncertainties in properties calculated with the equation of state are summarized in the conclusions.

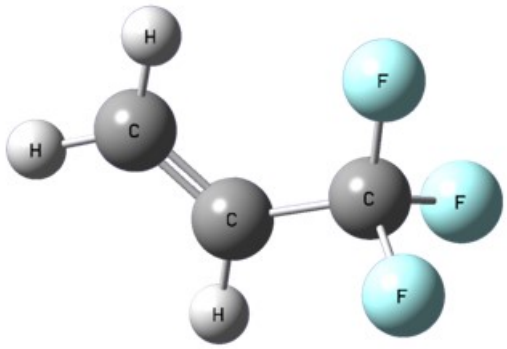

Fig. 1 Molecular structure of R-1243zf obtained from the geometry optimization with Gaussian 09 [10] (Calculation method: RB3LYP, Basic set: CC-pVDZ)

2 FUNDAMENTAL CONSTANTS

Table 1 lists the fundamental constants of R-1243zf. All properties are calculated from the equation of state developed in this work, except the molar mass M, molar gas constant R, critical temperature T_c, and triple-point temperature T_{tp}. Accurate values for the critical parameters are necessary to formulate reliable equations of state since they are often used as the reducing parameters for the independent variables. Higashi and Sakoda [11] experimentally determined the critical temperature and density of R-1243zf, which are

376.93 ± 0.01 K and 414 ± 3 kg $\cdot$ m^{-3}. This critical temperature was used as the reducing temperature for the equation of state. Experimental critical densities generally involve larger uncertainties than those in critical temperatures due to the infinite compressibility at the critical point and the difficulty of reaching thermodynamic equilibrium; this work used the critical density of Higashi and Sakoda [11] as an initial value for the reducing density, which was then slightly adjusted during the fitting of the equation of state. This allows for better representation of densities and vapor pressures near the critical point. The final value of the critical density was determined as 4.3 mol $\cdot$ dm^{-3} (approximately 413 kg $\cdot$ m^{-3}). Higashi and Sakoda [11] calculated the critical pressure as 3.518 MPa from the extrapolation of the vapor pressure correlation [12] to the critical temperature. The critical pressure calculated from the final equation of state (the pressure at 376.93 K and 4.3 mol $\cdot$ dm^{-3}) is 3.5137 MPa.

Di Nicola et al. [13] measured the triple-point temperature of R-1243zf as 122.8 ± 1.0 K. Tomassetti et al. [14] obtained two triple-point temperatures with different apparatuses, which are 122.35 ± 0.2 K and 122.6 ± 1.0 K. This work adopted 122.35 K as the triple-point temperature since it includes the lowest uncertainty. The value is used as the lower temperature limit for the applicable range of the equation of state. The vapor pressure at the triple-point temperature is calculated as 3.728×10^{-4} kPa with the final equation of state.

Table 1 Fundamental constants and other characteristic properties of R-1243zf[a]

Property	Symbol	Value	Unit	Reference
CAS number		677-21-4		
Chemical formula		$C_3H_3F_3$		
Molar mass	M	96.05113	$g \cdot mol^{-1}$	[15]
Molar gas constant	R	8.314462618	$J \cdot mol^{-1} \cdot K^{-1}$	[16]
Critical temperature	T_c	376.93	K	[11]
Critical pressure	p_c	3.5137	MPa	
Critical density	ρ_c	4.3	$mol \cdot dm^{-3}$	
Triple-point temperature	T_{tp}	122.35	K	[14]
Triple-point pressure	p_{tp}	3.728×10^{-4}	kPa	
Saturated liquid density at triple point	ρ'_{tp}	14.543	$mol \cdot dm^{-3}$	
Saturated vapor density at triple point	ρ''_{tp}	3.664×10^{-7}	$mol \cdot dm^{-3}$	
Normal boiling point temperature	T_b	247.666	K	
Saturated liquid density at normal boiling point	ρ'_b	11.572	$mol \cdot dm^{-3}$	
Saturated vapor density at normal boiling point	ρ''_b	0.05160	$mol \cdot dm^{-3}$	
Reference temperature for ideal gas properties	T_0	273.15	K	
Reference pressure for ideal gas properties	p_0	0.001	MPa	
Reference ideal-gas enthalpy at T_0	h°_0	39116.723279	$J \cdot mol^{-1}$	
Reference ideal-gas entropy at T_0 and p_0	s°_0	214.74827915	$J \cdot mol^{-1} \cdot K^{-1}$	
Acentric factor	ω	0.2595		

[a]All properties in this table were determined in this work, except M, R, T_c, and T_{tp}.

3 ANCILLARY EQUATIONS

Ancillary equations for the vapor pressure and saturated liquid and vapor densities are given here, which were correlated based on values calculated from the final equation of state. They provide rapid calculations of the saturation properties and also give excellent initial guesses for the iterative process to find rigorous solutions from the equation of state based on the Maxwell criteria. The ancillary equations fulfill the requirements stated by Lemmon and

Goodwin [17] for vapor pressure correlations and by Gao et al. [18] for saturated liquid and vapor density correlations. Table 2 summarizes the coefficients N_i of the equations. Figure 2 shows relative deviations in values calculated with the ancillary equations from the Maxwell solutions of the final equation of state.

The equation for the vapor pressure p_s is

$$\ln\left(\frac{p_\mathrm{s}}{p_\mathrm{c}}\right) = \frac{T_\mathrm{c}}{T}\left(N_1\theta + N_2\theta^{1.5} + N_3\theta^{2.32} + N_4\theta^{4.07} + N_5\theta^{15.4}\right), \qquad (1)$$

where p_c is the critical pressure (3.5137 MPa), T_c is the critical temperature (376.93 K), and $\theta = 1 - T/T_\mathrm{c}$. Equation 1 is valid at temperatures from the triple point (122.35 K) to the critical temperature, with a relative average deviation of 0.0015 % from the rigorous Maxwell solutions. At temperatures above 350 K, higher deviations of up to 0.01 % are sometimes observed. The saturated liquid and vapor densities (ρ' and ρ'') are calculated from the equations

$$\frac{\rho'}{\rho_\mathrm{c}} = 1 + N_1\theta^{0.258} + N_2\theta^{0.82} + N_3\theta^{1.43} + N_4\theta^{2.11} + N_5\theta^{8.4} \qquad (2)$$

and

$$\ln\left(\frac{\rho''}{\rho_\mathrm{c}}\right) = N_1\theta^{0.28} + N_2\theta^{0.96} + N_3\theta^{2.78} + N_4\theta^{5.38} + N_5\theta^{9.36} + N_6\theta^{16.6}, \quad (3)$$

where ρ_c is the critical density (4.3 $\mathrm{mol \cdot dm^{-3}}$). Equations 2 and 3 are applicable in the range from the triple-point temperature to the critical temperature, with relative average deviations from the rigorous Maxwell solutions of 0.0010 % in Eq. 2 and 0.0015 % in Eq. 3. Larger deviations up to 0.02 % are observed in calculated saturated vapor densities at temperatures above 370 K.

Table 2 Coefficients of Eqs. 1, 2, and 3

	Eq. 1	Eq. 2	Eq. 3
N_1	−7.2325	1.2627	−1.6776
N_2	1.3165	2.6023	−6.5573
N_3	−0.8189	−2.4034	−14.195
N_4	−3.5606	1.6370	−33.488
N_5	−3.4861	0.29192	−49.802
N_6			−127.65

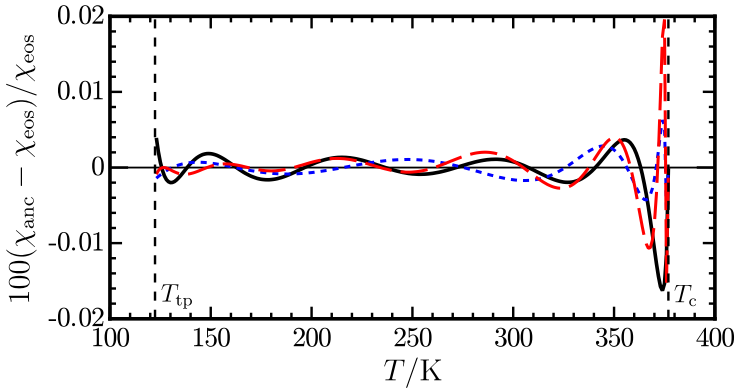

Fig. 2 Relative deviations in vapor pressures, saturated liquid densities, and saturated vapor densities calculated with the ancillary equations (χ_{anc}) from the Maxwell solution of the final equation of state (χ_{eos}): (black solid line) vapor pressure; (blue dotted line) saturated liquid density; (red dashed line) saturated vapor density.

4 EQUATION OF STATE

4.1 Overview

The equation of state developed in this work is expressed explicitly in the Helmholtz energy as the fundamental property with independent variables of temperature and density, which is given by

$$\frac{a(T,\rho)}{RT} = \alpha(\tau,\delta) = \alpha^{\circ}(\tau,\delta) + \alpha^{r}(\tau,\delta), \tag{4}$$

where a is the molar Helmholtz energy, α is the dimensionless Helmholtz energy, R is the molar gas constant, $\tau = T_c/T$ is the reciprocal reduced temperature, and $\delta = \rho/\rho_c$ is the reduced density. The value of R used in this work is

8.314462618 $\mathrm{J \cdot mol^{-1} \cdot K^{-1}}$, which is the CODATA recommended value based on the 2018 adjustment [16]. The dimensionless Helmholtz energy α is split into an ideal-gas part α° representing ideal-gas properties and a residual part α^r corresponding to the influence of intermolecular forces between molecules. The Helmholtz energy given by Eq. 4 is one of four fundamental functions in thermodynamics, and therefore all thermodynamic properties in the single phase are calculated from the derivatives with respect to temperature and density. Equations to calculate various thermodynamic properties from the Helmholtz energy are given in the literature, e.g. Span [19] and Lemmon et al. [20]. The location of the saturation boundaries requires an iterative solution of the physical constraints on saturation (the Maxwell criteria). Kretzschmar et al. [21], Span [19], and Akasaka [22] discuss robust numerical algorithms to correctly obtain the Maxwell solutions.

4.2 Ideal-gas Helmholtz Energy

The dimensionless ideal-gas Helmholtz energy α° is given by

$$\alpha^\circ(\tau,\delta) = \frac{h_0^\circ \tau}{RT_\mathrm{c}} - \frac{s_0^\circ}{R} - 1 + \ln\frac{\delta\tau_0}{\delta_0\tau} - \frac{\tau}{R}\int_{\tau_0}^{\tau}\frac{c_p^\circ}{\tau^2}\mathrm{d}\tau + \frac{1}{R}\int_{\tau_0}^{\tau}\frac{c_p^\circ}{\tau}\mathrm{d}\tau, \qquad (5)$$

where c_p° is the ideal-gas isobaric heat capacity, $\tau_0 = T_\mathrm{c}/T_0$, $\delta_0 = \rho_0/\rho_\mathrm{c} = p_0/(RT_0\rho_\mathrm{c})$, T_0 is the temperature at a reference state, p_0 is a reference pressure for the ideal-gas properties, and ρ_0 is the ideal-gas density at (T_0, p_0). The c_p° equation developed in this work for R-1243zf has the form

$$\frac{c_p^\circ}{R} = n_0^\circ + \sum_{i=1}^{2} n_i^\circ \left(\frac{m_i^\circ}{T}\right)^2 \frac{\exp(m_i^\circ/T)}{[\exp(m_i^\circ/T)-1]^2}\,, \qquad (6)$$

where the coefficients n_i° and exponents m_i° are given in Table 3. Equation 6 was obtained from simultaneously fitting together the ideal and residual parts so that the final equation of state represents experimental vapor-phase sound speed data almost within their expanded uncertainties. The fitting was made under two boundary conditions based on statistical mechanics; the value of c_p° should go to $4R$ at 0 K and asymptotically close to near $(4 + 21)R$ at extremely high temperatures [23]. Figure 3 shows c_p° values calculated from Eq. 6 over a wide range of temperature, as well as the experimental data [24]. The average deviation between experimental and calculated values is 0.52 %, which is comparable to the expanded uncertainties ($k = 2$) evaluated by the author (0.5 %).

Applying Eq. 6 to Eq. 5, the following expression is used for calculating the dimensionless ideal-gas Helmholtz energy:

$$\alpha^\circ(\tau,\delta) = \ln\delta + n_3^\circ + n_4^\circ\tau + (n_0^\circ - 1)\ln\tau + \sum_{i=1}^{2} n_i^\circ \ln\left[1 - \exp\left(-\frac{m_i^\circ\tau}{T_\mathrm{c}}\right)\right]. \quad (7)$$

The values of n_3° and n_4°, which are also given in Table 3, were determined so that the specific enthalpy and entropy of the saturated liquid state at 0 °C are 200 $\mathrm{kJ\cdot kg^{-1}}$ and 1 $\mathrm{kJ\cdot kg^{-1}\cdot K^{-1}}$, corresponding to the common convention of the refrigeration industry. Additional digits are given to these coefficients in order to better reproduce these enthalpy and entropy values specified at the reference state.

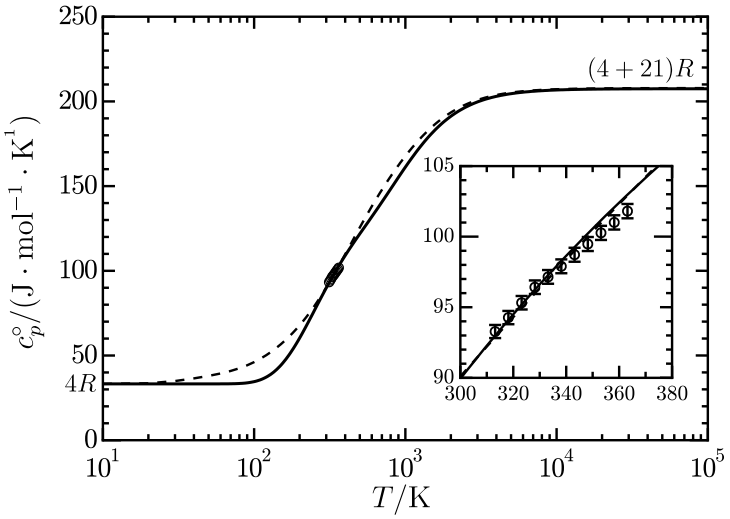

Fig. 3 Ideal-gas isobaric heat capacity (c_p°) of R-1243zf: (◯) Chen et al. [24], (dashed line) Gaussian 09 [10] (Calculation method: RB3LYP, Basic set: CC-pVDZ), (solid line) Eq. 6.

Table 3 Coefficients and exponents of Eqs. 6 and 7 for R-1243zf

i	n_i°	m_i°
0	4.0	-
1	13.285	877.6
2	7.67	3562.5
3	−12.2722866918	-
4	8.2858157407	-

4.3 Residual Helmholtz Energy

An equation to express the residual Helmholtz energy is normally determined by fitting an empirical functional form to experimental data. Following the recent fashion in the development of accurate equations of state for industrial fluids, this work used the functional form:

$$\alpha^{\mathrm{r}}(\tau,\delta) = \sum n_i \tau^{t_i} \delta^{d_i} + \sum n_i \tau^{t_i} \delta^{d_i} \exp(-g_i \delta^{e_i}) + \sum n_i \tau^{t_i} \delta^{d_i} \exp\left[-\eta_i(\delta-\varepsilon_i)^2 - \beta_i(\tau-\gamma_i)^2\right], \quad (8)$$

where the first, second, and final summations are called polynomial, exponential, and Gaussian bell-shaped (simply Gaussian) terms, respectively. This work determined the coefficients (n_i), exponents (t_i and d_i), and other parameters (g_i, e_i, η_i, ε_i, β_i, and γ_i; the last four parameters are called "Gaussian parameters") by nonlinear least-squares fitting. While g_i was always set to 1 in recent equations for refrigerants [9,25–28], it was adjusted between 0 and 1 in this work to obtain more flexibility. Derivatives of the exponential terms are given in the Appendix. The reduction and addition of the number of terms were made manually based on new discoveries in the structure of the terms and the ranges of the parameters over the past few years.

The nonlinear least-squares fitting employed in this work was originally developed by Lemmon and Jacobsen [29], where not only deviations from experimental data are minimized, but various thermodynamic constraints are applied so that the equation obeys physically correct behavior over wide ranges of temperature and pressure. For example, the constraints that the slope and curvature of the critical isotherm are both zero at the critical point are always considered while fitting. Derived properties such as virial coefficients and heat capacities are controlled in order that their value, slope, curvature, and, in some cases, third and fourth derivatives, exhibit reasonable behavior in all regions. Collaborations between correlators over the last decade [9,18,20,25–28, 30–32] made the fitting technique greatly progress. Romeo and Lemmon [33] present a list of the thermodynamic constraints to be considered. In addition to the thermodynamic constraints, the most recent work also regulates adjustable

ranges for the coefficients, exponents, and Gaussian parameters. For example, η_i and ε_i should be in the ranges of $0.2 \leq \eta_i \leq 3$ and $-0.5 \leq \varepsilon_i \leq 1.1$. These regulations are empirical but important to develop reliable equations with less intercorrelation and higher numerical stability in extrapolated regions. Akasaka and Lemmon [27] and Lemmon and Akasaka [28] gave an overview of the fitting techniques taking adjustable ranges of fitted parameters into account.

The final form for the residual Helmholtz energy of R-1243zf is

$$\alpha^{\mathrm{r}}(\tau,\delta) = \sum_{i=1}^{6} n_i \tau^{t_i} \delta^{d_i} + \sum_{i=7}^{11} n_i \tau^{t_i} \delta^{d_i} \exp(-g_i \delta^{e_i}) + \sum_{i=12}^{15} n_i \tau^{t_i} \delta^{d_i} \exp\left[-\eta_i(\delta-\varepsilon_i)^2 - \beta_i(\tau-\gamma_i)^2\right], \tag{9}$$

where the coefficients, exponents, and Gaussian parameters are given in Table 4. By introducing values of g_i that are not equal to 1, the total number of terms (15 in this work) is 2 or 3 less than those of equations recently developed for refrigerants [26–28,32]. In order to avoid the intercorrelation in modeling virial coefficients, positive coefficients are given to terms with $0 < t_i \leq 0.9$, and negative coefficients are assigned to terms with $t_i > 0.9$. The larger number of digits is given to n_3 and n_4 to make the slope and curvature of the critical isotherm exactly zero at the critical point. This is demonstrated in Section 6.

Table 4 Coefficients and exponents of Eq. 9

i	n_i	t_i	d_i	e_i	g_i	η_i	β_i	γ_i	ε_i
1	0.02626021	1.	4						
2	0.701348	0.12425	1						
3	−0.6180002748076	1.0096	1						
4	0.1916400159007	0.271875	2						
5	0.0762	0.405	3						
6	−0.795	1.07288	2						
7	−0.8537	1.45525	1	1	1				
8	−0.3531	2.105	1	2	1				
9	−0.07971	6.07	1	3	1				
10	−0.05411	5.794375	2	3	0.66				
11	−0.0424	4.094	3	3	0.33				
12	−0.06774	1.029	1			0.78	0	1	1.09375
13	−0.01032	1.65	2			2.796	0	1	1.0392
14	−0.1184	1.62	1			1.643	1.86	0.80625	−0.3076
15	−0.1135	1.653125	1			3.03	2.03	1.16	−0.426

5 AVAILABLE EXPERIMENTAL DATA AND COMPARISONS TO THE EQUATION OF STATE

Table 5 summarizes the experimental data currently available for R-1243zf and their average absolute deviations (AADs) in calculated values from the equation of state. The AAD in any property X is defined as

$$\mathrm{AAD}_X = \frac{100}{N_{\mathrm{exp}}} \sum_{i=1}^{N_{\mathrm{exp}}} \left| \frac{X_{i,\,\mathrm{exp}} - X_{i,\,\mathrm{calc}}}{X_{i,\,\mathrm{exp}}} \right|, \tag{10}$$

where N_{exp} is the number of data points in a dataset, $X_{i,\,\mathrm{exp}}$ is the ith experimental value, and $X_{i,\,\mathrm{calc}}$ is the calculated value at the state conditions for $X_{i,\,\mathrm{exp}}$. For (p, ρ, T) data, the deviations are given in terms of density values. For comparisons, AADs from the first and second equations [8,9] are given in this table.

Table 5 Available experimental data of R-1243zf and their average deviations from the equations of state

			Range		AAD (%)		
Author (year)	L/V	N	T/K	p/MPa	1st EOS [8]	2nd EOS [9]	This work
Vapor pressure							
Daubert et al. [34]		38	256–374	0.14–3.31	1.72	1.72	1.65
Brown et al. [35] (ITC-CNR)		55	247–353	0.10–2.21	0.12	0.15	0.16
Brown et al. [35] (UnivPM)		28	234–373	0.05–3.26	0.15	0.17	0.18
Higashi et al. [12]		17	310–375	0.82–3.39	0.03	0.03	0.12
Yang et al. [2]		17	273–353	0.27–2.20	0.16	0.16	0.15
Yin et al. [36]		26	253–376	0.13–3.46	0.12	0.11	0.04
Li et al. [3]		6	273–313	0.27–0.88	0.21	0.28	0.13
Fedele et al. [4]		5	283–323	0.37–1.13	0.24	0.30	0.13
Saturated liquid density							
Higashi and Sakoda [11]		7	360–377		0.87	0.71	1.26
Saturated vapor density							
Higashi and Sakoda [11]		7	367–377		1.23	1.22	2.32
(p, ρ, T) data[a]							
Di Nicola et al. [37]	L	302	283–353	1.30–34.5	0.04	0.03	0.03
Di Nicola et al. [37]	V	99	278–368	0.24–0.91	0.59	0.60	0.67
Higashi and Sakoda [11]	L	45	328–425	2.18–6.90	0.29	0.07	0.41
Higashi and Sakoda [11]	V	37	323–430	1.07–4.76	2.05	0.98	0.86
Yin et al. [36]	V	128	253–368	0.11–2.89	0.30	0.35	0.14
Ding et al. [38]	L	86	253–302	1.59–9.50	0.08	0.01	0.08
Tenardi et al. [39]	L	109	203–294	1.04–15.2	0.20	0.33	0.08
Peng et al. [6]	V	74	313–403	0.48–3.58	0.98	0.68	0.28
Sound speed							
Chen et al. [24]	V	92	313–363	0.17–0.98	0.36	0.20	0.03
Second acoustic virial coefficient							
Chen et al. [24]		11	313–363		3.88	2.27	1.31
Isochoric heat capacity							
Sheng et al. [40]	L	64	300–351	1.58–10.2	1.12	2.41	0.95
Ding et al. [38]	L	86	253–302	1.59–9.50	4.03	2.43	0.94
Isobaric heat capacity							
Sheng et al. [41]	L	65	232–284	2.00–8.04	5.34	2.53	1.79
Ideal-gas isobaric heat capacity							
Chen et al. [24]		11	313–363		0.74	0.60	0.52

[a]Deviations in density are shown for (p, ρ, T) data.

5.1 Saturation Properties

Eight datasets are currently available for the vapor pressure of R-1243zf. Figure 4 shows relative deviations and absolute differences in the experimental vapor pressures from values calculated with the equation of state. All data are less scattered and are almost consistent with each other, except for the earliest dataset of Daubert et al. [34], which is excluded in the overall statistical analysis presented here. For a total of 154 data points, 90 % of them are represented within 2 kPa, and the overall averages of relative deviations and absolute differences are 0.136 % and 0.960 kPa, which are comparable to the typical expanded experimental uncertainty ($k = 2$). A similar trend is observed in the data of Brown et al. [35] (ITC-CNR), Brown et al. [35] (UnivPM), Higashi et al. [12], and Yang et al. [2]. These data show negative deviations at temperatures below 300 K and positive deviations at higher temperatures, which are generally within 2 kPa. The data of Yin et al. [36] agree very well with calculated values over the whole temperature range. The AAD in the data is 0.04 % and the differences are within 2 kPa other than a data point at 363 K. The most recent data of Li et al. [3] and Fedele et al. [4] show systematic negative deviations, but the differences are always within 2 kPa.

Figure 5 shows absolute differences between the saturation temperatures as a function of pressure; such differences are particularly applicable for heat transfer analyses where the saturation temperature is calculated based on a measured pressure in a heat exchanger. The overall average difference is

0.046 K, and 93 % of the differences between the experimental temperatures and calculated values are within 0.1 K.

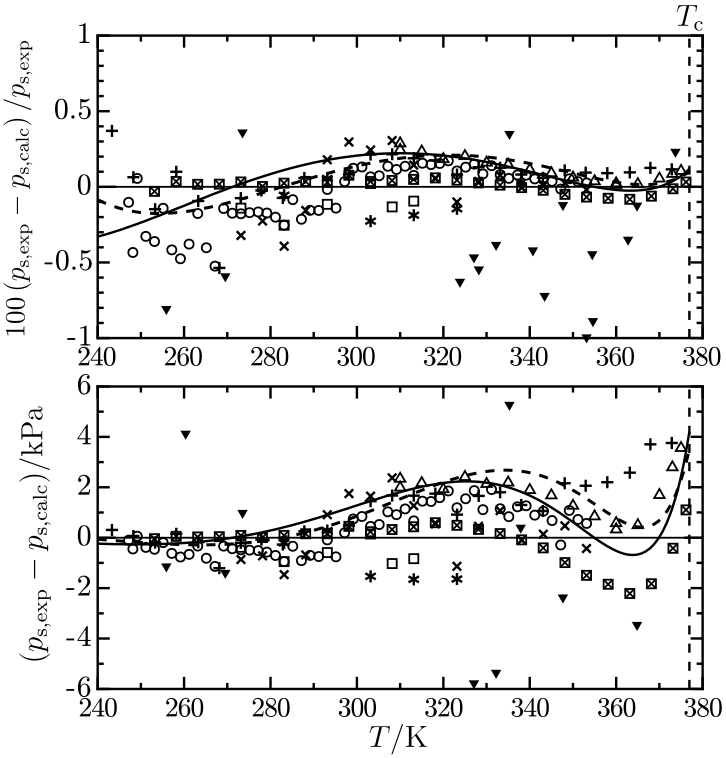

Fig. 4 Relative deviations (top panel) and absolute differences (bottom panel) in experimental vapor pressures from values calculated with the equation of state: (▼) Daubert et al. [34], (◯) Brown et al. [35] (ITC-CNR), (+) Brown et al. [35] (UnivPM), (△) Higashi et al. [12], (×) Yang et al. [2], (⊠) Yin et al. [36], (□) Li et al. [3], (∗) Fedele et al. [4], (dashed line) 1st EOS [8], (solid line) 2nd EOS [9].

Although available experimental data are limited for the saturated liquid and vapor densities, calculated values from the equation of state should be reliable due to the consistent vapor pressures and (p, ρ, T) data used in the fitting process. Figure 6 confirms this, where the saturation boundary obtained from the equation of state is displayed on a T–ρ diagram along with experimental,

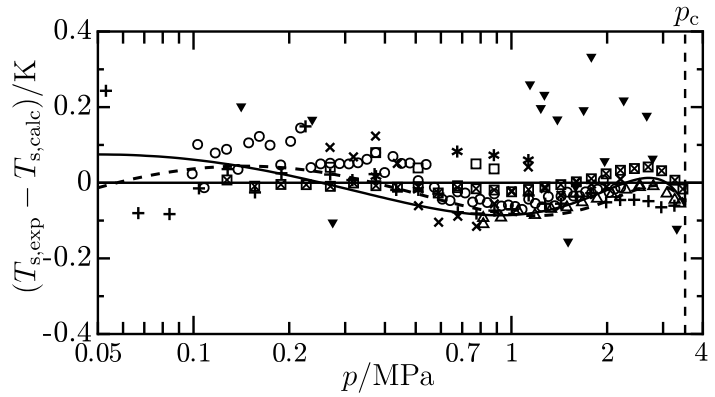

Fig. 5 Absolute differences between experimental saturation temperatures and values calculated with the equation of state: (▼) Daubert et al. [34], (◯) Brown et al. [35] (ITC-CNR), (+) Brown et al. [35] (UnivPM), (△) Higashi et al. [12], (×) Yang et al. [2], (⊠) Yin et al. [36], (□) Li et al. [3], (∗) Fedele et al. [4], (dashed line) 1st EOS [8], (solid line) 2nd EOS [9].

correlated, or simulation data for the saturated liquid and vapor densities. The correlation by Di Nicola et al. [37] for the saturated liquid density, which was obtained by the extrapolation of their experimental compressed liquid densities, shows good agreement with the saturation boundary from the equation of state at temperatures from 230 K to 375 K. The AAD between values from the correlation and the equation of state is 0.15 %. The saturated liquid and vapor densities measured by Higashi and Sakoda [11] and those with the GEMC simulation of Raabe [42] agree well with the saturation boundary calculated from the equation of state.

5.2 (p, ρ, T) data

Eight experimental datasets are currently available for the (p, ρ, T) behavior. Their distributions on a p–T diagram are given in Figure 7, along with the vapor pressure curve calculated from the equation of state. Figure 8 shows

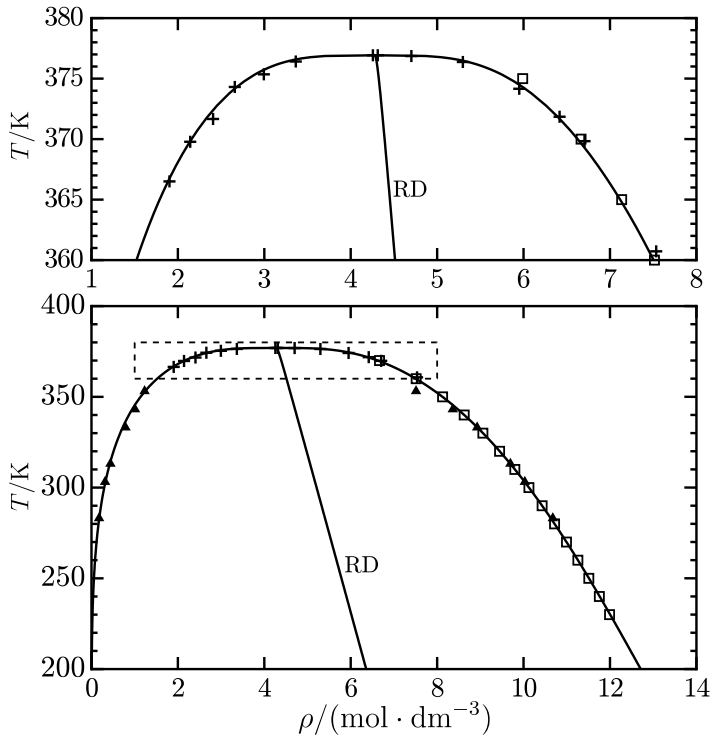

Fig. 6 Saturation boundary calculated from the equation of state and related data for the saturated liquid and vapor densities: (□) Di Nicola et al. [37] (correlation based on compressed liquid densities), (+) Higashi and Sakoda [11] (experimental), (▲) Raabe [42] (GEMC simulation), RD: Rectilinear diameter.

comparisons between the experimental densities and values calculated from the equation of state in different temperature intervals.

For the liquid phase, there are 542 data points in four datasets, and their overall AAD is 0.08 %. The data of Di Nicola et al. [37], Ding et al. [38], and Tenardi et al. [39] excellently agree with the equation. The AADs are 0.03 %, 0.08 %, and 0.08 %, respectively. The maximum deviation in the equation at the highest pressure (34.5 MPa) compared to the data of Di Nicola et al. [37] is 0.13 %, and that at the lowest temperature (203 K) compared to the data of Tenardi et al. [39] is 0.20 %. The data of Higashi and Sakoda [11] show larger

deviations; the AAD is 0.41 %, but decreases to 0.10 % if the data along the critical isochore are excluded. Some data points on the critical isochore show deviations larger than 1 %.

A total of 338 data points are available for the vapor and supercritical regions, and the overall AAD is 0.42 %. The data of Di Nicola et al. [37] and Higashi and Sakoda [11] are scattered, and the AADs are 0.67 % and 0.86 %, respectively, which are larger than their experimental uncertainties (about 0.15 %). Deviations in some data points exceed 1 %. The data of Yin et al. [36] and Peng et al. [6] show better agreement with the equation. The AADs are 0.14 % and 0.28 %, respectively, which are slightly larger than their typical uncertainties (0.10–0.12 %) but sufficiently close enough for engineering applications. All data points are represented within 0.5 %, except in the critical region, where deviations up to 1.3 % are sometimes observed.

5.3 Sound speed

Chen et al. [24] measured vapor-phase sound speeds with a cylindrical resonator at temperatures from 313 K to 363 K and pressures up to 0.98 MPa, which are the only available sound speed data for R-1243zf at this time. Figure 9 shows deviations in the data from values calculated with the equation of state. All data points are represented within 0.1 %, and the AAD is 0.03 %; this slightly exceeds the experimental uncertainty (0.018 %), but it is considerably improved over the former two equations. The second acoustic virial

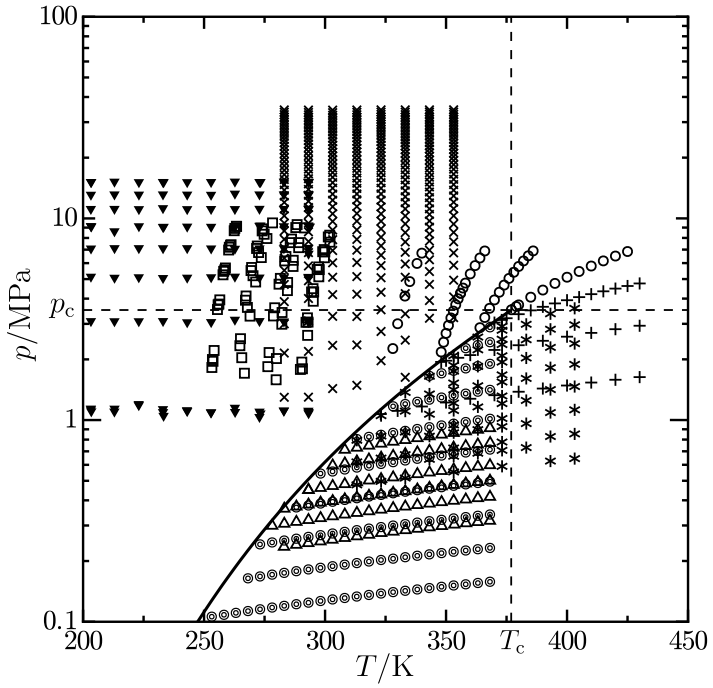

Fig. 7 Distribution of experimental (p, ρ, T) data of R-1243zf: (×) Di Nicola et al. [37] (L), (△) Di Nicola et al. [37] (V), (◯) Higashi and Sakoda [11] (L), (+) Higashi and Sakoda [11] (V), (◎) Yin et al. [36] (V), (□) Ding et al. [38] (L), (▼) Tenardi et al. [39] (L), (∗) Peng et al. [6] (V).

coefficient B_a is given by Gillis and Moldover [43] as follows:

$$B_a = 2B + 2(\kappa^\circ - 1)TB_t + \frac{(\kappa^\circ - 1)^2}{\kappa^\circ}T^2 B_{tt}, \tag{11}$$

where B is the second virial coefficient, B_t and B_{tt} are the first and second derivatives of B with respect to temperature, and κ° is the ratio of the isobaric to the isochoric heat capacities in the ideal-gas state. The second virial

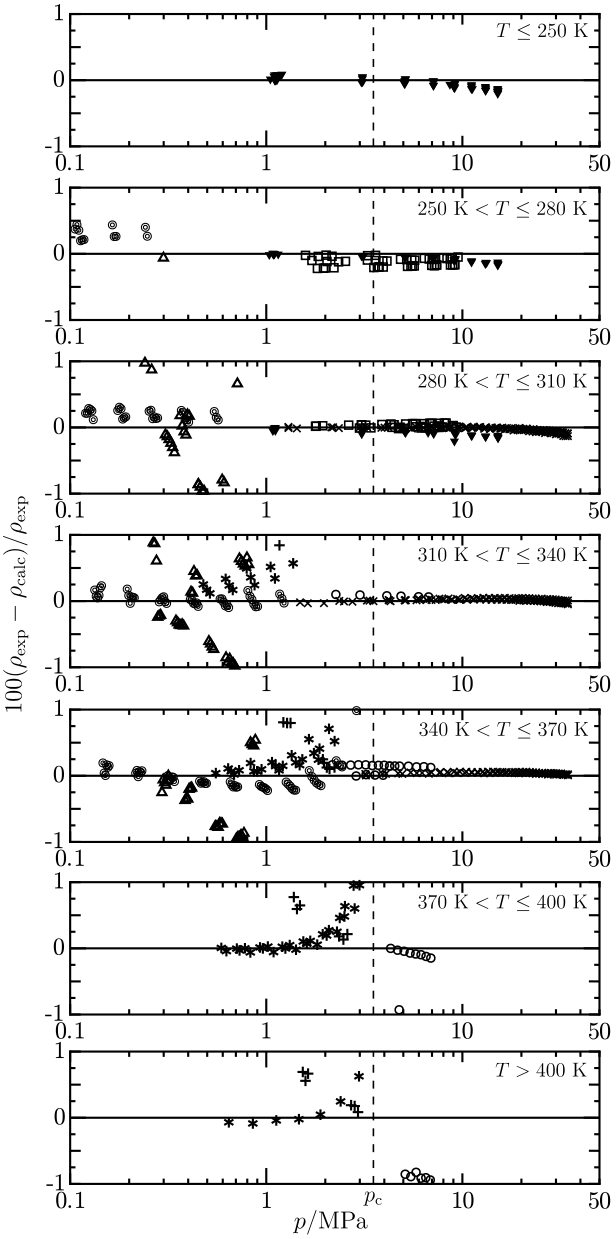

Fig. 8 Relative deviations in experimental densities from values calculated with the equation of state: (×) Di Nicola et al. [37] (L), (△) Di Nicola et al. [37] (V), (◯) Higashi and Sakoda [11] (L), (+) Higashi and Sakoda [11] (V), (⊙) Yin et al. [36] (V), (□) Ding et al. [38] (L), (▼) Tenardi et al. [39] (L), (∗) Peng et al. [6] (V).

coefficient and its temperature derivatives are calculated as

$$B = \lim_{\rho \to 0} \left[\frac{\delta}{\rho} \left(\frac{\partial \alpha^{\mathrm{r}}}{\partial \delta} \right)_{\tau} \right], \tag{12}$$

$$B_t = \frac{\mathrm{d}B}{\mathrm{d}T} = \lim_{\rho \to 0} \left[-\frac{\tau \delta}{\rho T} \left(\frac{\partial^2 \alpha^{\mathrm{r}}}{\partial \tau \partial \delta} \right) \right], \text{ and} \tag{13}$$

$$B_{tt} = \frac{\mathrm{d}^2 B}{\mathrm{d}T^2} = \lim_{\rho \to 0} \left\{ \frac{\tau \delta}{\rho T^2} \left[2 \left(\frac{\partial^2 \alpha^{\mathrm{r}}}{\partial \tau \partial \delta} \right) + \tau \left(\frac{\partial^3 \alpha^{\mathrm{r}}}{\partial \tau^2 \partial \delta} \right) \right] \right\}. \tag{14}$$

Experimental B_{a} data [24] and values calculated from three equations of state are given in Figure 10. The equation developed in this work generally represents the behavior of B_{a}.

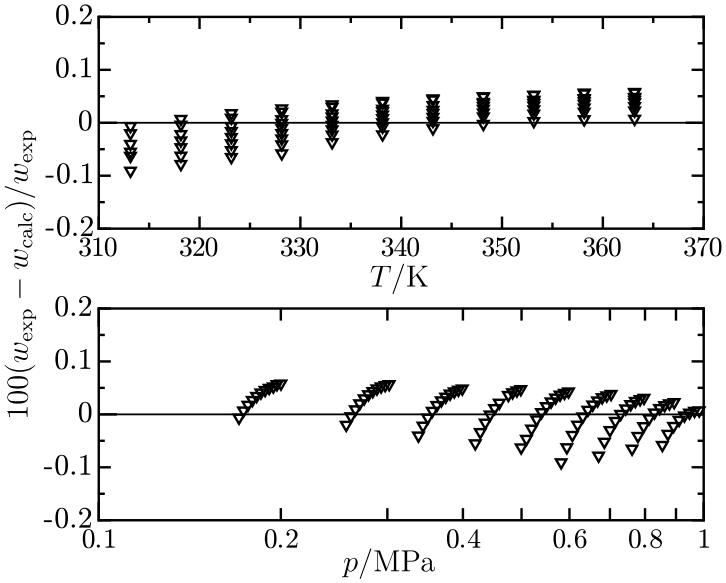

Fig. 9 Relative deviations between experimental vapor-phase sound speeds and values calculated with the equation of state: (▽) Chen et al. [24]

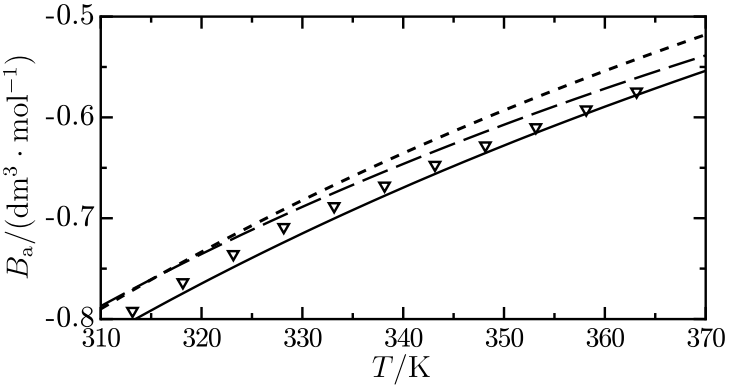

Fig. 10 Second acoustic virial coefficient: (▽) Chen et al. [24], (dotted line) 1st EOS [8], (dashed line) 2nd EOS [9], (solid line) This work.

5.4 Caloric data

Experimental data for the isochoric heat capacity were reported by Sheng et al. [40] and Ding et al. [38] for the liquid phase. Figure 11 shows deviations in the data from values calculated with the equation of state. Although systematic negative deviations are observed in the data above 6 MPa, 91 % of the data points are represented within 2 %. The AADs in the data of Sheng et al. [40] and Ding et al. [38] are 0.95 % and 0.94 %, respectively, which are less than their typical experimental uncertainties (1.8 %, $k = 2$). Experimental data for the liquid-phase isobaric heat capacity [41], which became available after the equation was established, show an AAD of 1.79 %; this is less than the experimental uncertainty (2.0 %, $k = 2$), and verifies the validity of other statements in this work about the low uncertainties in other properties and in regions where data are not available.

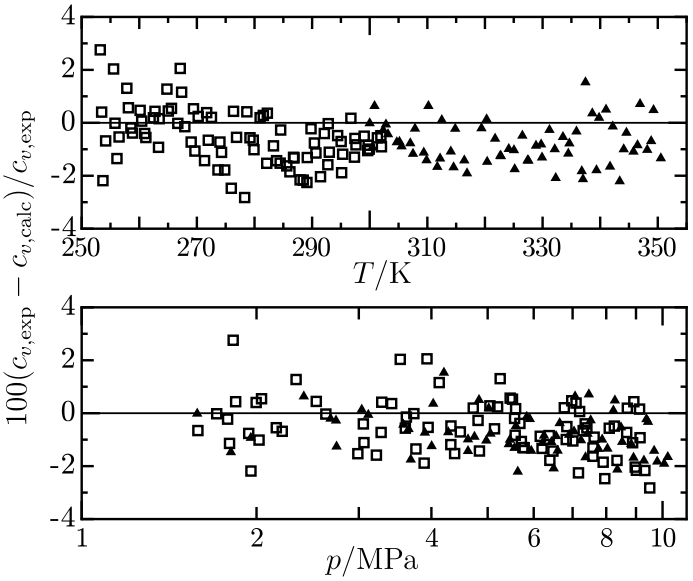

Fig. 11 Relative deviations in experimental data for the isochoric heat capacity from values calculated with the equation of state: (▲) Sheng et al. [40], (□) Ding et al. [38]

6 EXTRAPOLATION BEHAVIOR OF THE EQUATION OF STATE

Several demonstrative plots of derived properties are shown here to verify the behavior of the equation of state in extrapolated or critical regions. This is particularly essential for equations of state based on experimental data within limited ranges, such as the equation developed in this work.

Plots are given first for the (p, ρ, T) properties, which are calculated from the first derivative of the Helmholtz energy with respect to density. Figure 12 shows the trend in pressure (calculated from the first density derivative) along isotherms up to extremely high temperatures and densities. All isotherms exhibit the physically correct shape; they should increase monotonically as density increases and become asymptotically close to a single line but never cross

each other. This behavior results from the first term with the highest density exponent ($d_1 = 4$), which becomes dominant at extremely high densities.

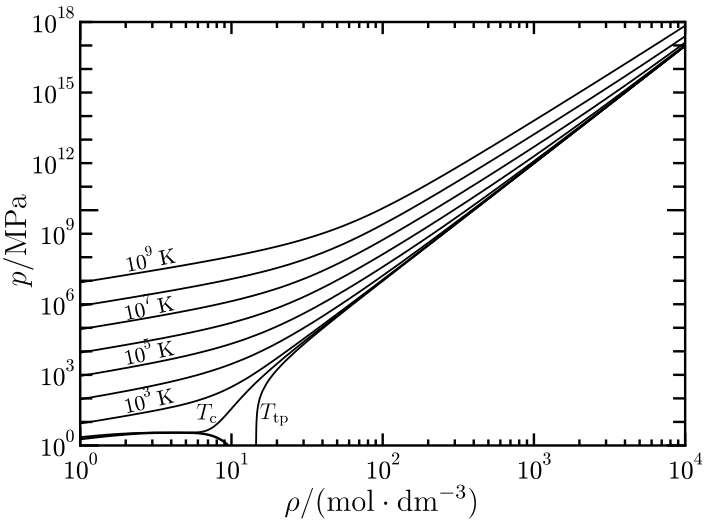

Fig. 12 Pressure versus density along isotherms at T_{tp}, T_c, 10^3 K, 10^4 K, 10^5 K, 10^6 K, 10^7 K, 10^8 K, and 10^9 K.

Virial coefficients, the most fundamental properties representing intermolecular forces in the vapor phase, are values of density derivatives of the residual Helmholtz energy in the limit of zero density, as given by Eq. 12. The theoretically expected behavior of the second, third, and fourth virial coefficients (B, C, and D) are as follows [44]: B and C (related to the first and second density derivatives) go to negative infinity at zero temperature, pass through zero at a moderate temperature, increase to a maximum, and approach zero at extremely high temperatures; D (related to the third density derivative) shows a similar trend to those in B and C, however, there is a second maximum with a smaller magnitude at a higher temperature. Changes in B, C, and D ob-

tained from the equation of state are shown in Figure 13, which demonstrates that the equation reproduces the theoretically expected behavior of the virial coefficients.

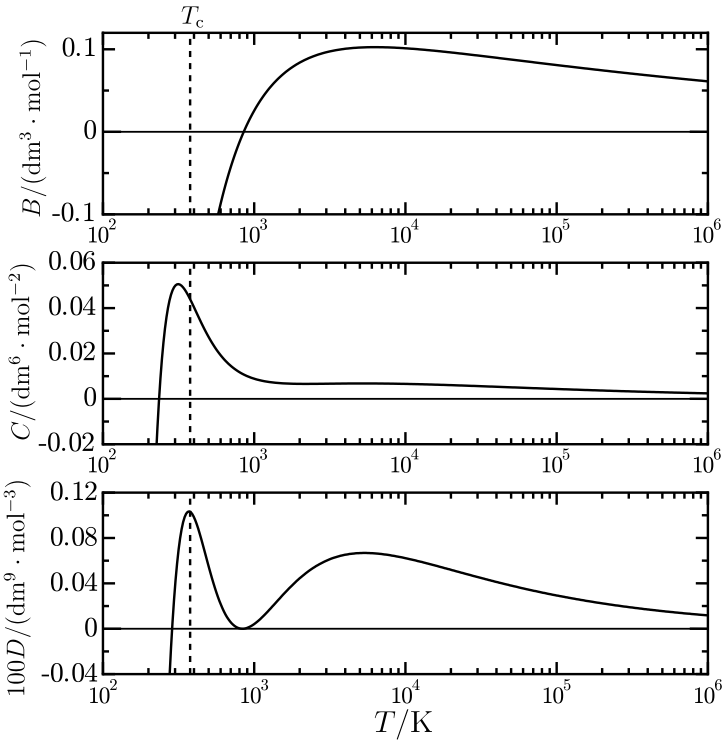

Fig. 13 Second, third, and fourth virial coefficients (B, C, and D) calculated from the equation of state.

It is an essential prerequisite for reliable equations of state to accurately reproduce the behavior of the critical isotherm. When displayed on a p-ρ diagram, it has positive slope and negative curvature at densities below ρ_c, and has positive slope and positive curvature at densities above ρ_c; therefore, ρ_c should be a distinct saddle point. Figure 14 shows a plot of the critical isotherms and the saturation lines calculated from the equation of state. The

behavior of the isotherm is overall reasonable, and incorrect slopes or curvatures are not observed. This is more closely verified in Figure 15, where the first and second derivatives of pressure with respect to density are plotted versus density in the vicinity of the critical point. These derivatives become exactly zero at ρ_c; this is due to additional digits given to the coefficients of the third and fourth terms of the residual Helmholtz energy.

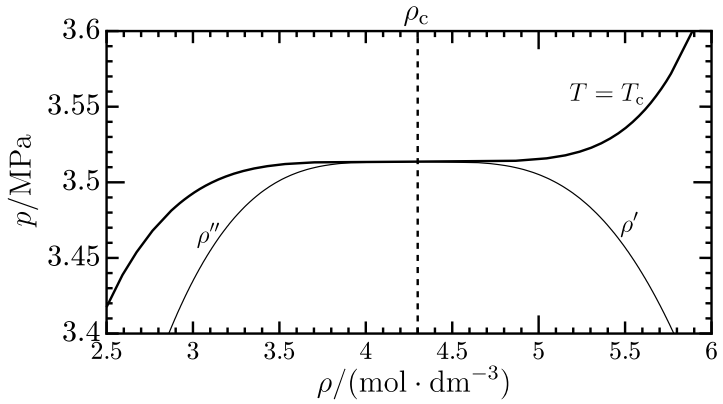

Fig. 14 Critical isotherm and saturation lines calculated from the equation of state.

Heat capacities and sound speeds are related to derivatives of the Helmholtz energy with respect to temperature and density, and plots of these properties are often used to examine the validity of these derivatives. Figure 16 shows the residual isochoric heat capacities c_v^r $(= c_v - c_v^\circ)$ calculated from the equation of state along various isobar and the saturation lines. All isobars exhibit reasonable shapes both in the critical and extrapolated regions, which means that the second temperature derivatives of the Helmholtz energy are correct (the isochoric heat capacity is calculated only from the second temperature derivative). The saturation lines should cross once at a temperature slightly

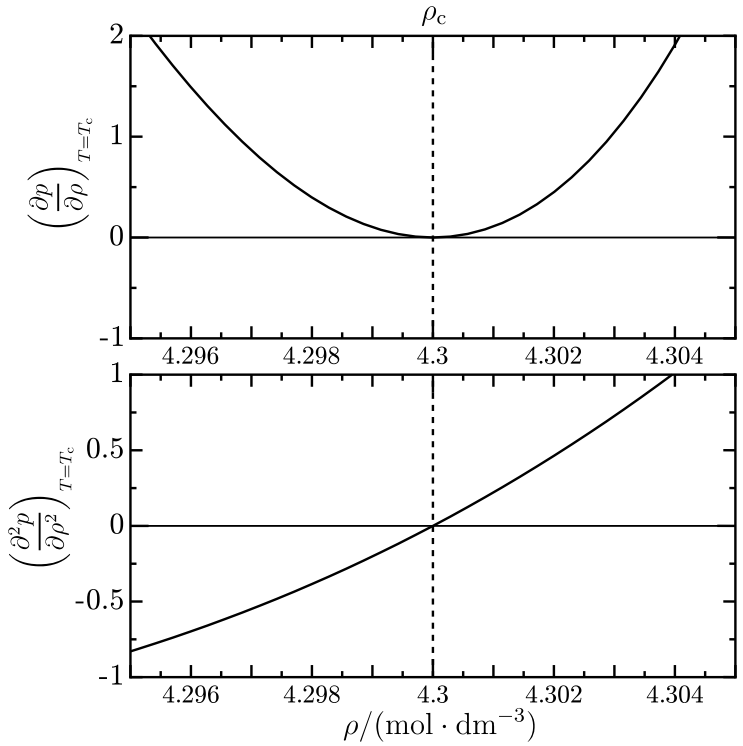

Fig. 15 First and second partial pressure derivatives with respect to density along the critical isotherm, calculated from the equation of state. The units of $(\partial p/\partial \rho)_{T=T_c}$ and $(\partial^2 p/\partial \rho^2)_{T=T_c}$ are $\mathrm{mPa}\cdot\mathrm{dm}^3\cdot\mathrm{mol}^{-1}$ and $\mathrm{kPa}\cdot\mathrm{dm}^6\cdot\mathrm{mol}^{-2}$, respectively.

below the critical temperature, and they should meet again at the critical temperature forming a distinct maximum [45,46]; this is observed in Figure 16.

In Figure 17, the sound speeds calculated from the equation of state are plotted versus temperature along isobars and the saturation lines. They follow the physically correct shape [45,46], i.e., the saturated liquid curve has a negative slope and exhibits a smooth arc when displayed on a logarithmic temperature scale. In contrast, the saturated vapor curve shows a change from a positive to a negative slope with increasing temperatures while maintaining negative curvature. The slopes of isobars are negative in the liquid phase and

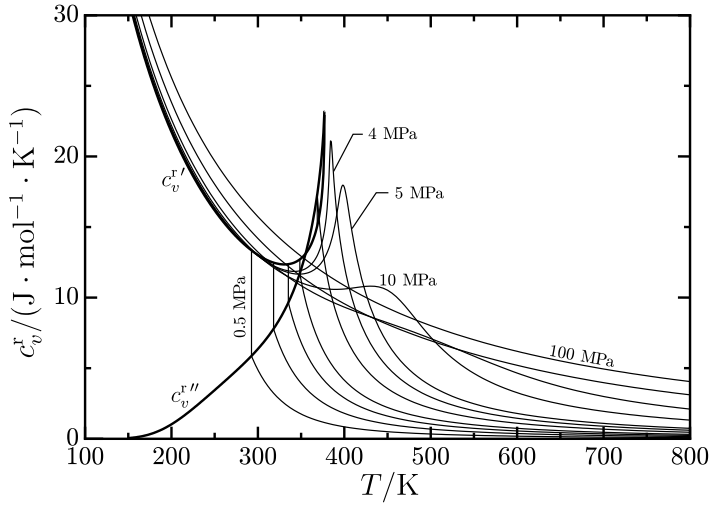

Fig. 16 Residual isochoric heat capacity c_v^{r} versus temperature diagram. Isobars are shown at pressures of 0.5 MPa, 1 MPa, 1.5 MPa, 2 MPa, 3 MPa, 4 MPa, 5 MPa, 10 MPa, 20 MPa, 50 MPa, 100 MPa, and the saturation boundaries.

positive in the vapor and supercritical regions, while the curvature remains positive everywhere. The physically-correct behavior of the sound speed shown in Fig. 17 implies that the second derivative of the Helmholtz energy with respect to temperature and density is also reasonably calculated, in addition to the first and second density derivatives.

The phase identification parameter (PIP) [47] is a product of the second or higher-order derivatives, and therefore very sensitive to underlying problems in equations of state. Figures 18 and 19 show changes in the PIP along isobars, isotherms, and the saturation boundary. The behavior of the PIP depicted in these figures follows the physically correct trends [45], for example, when plotted versus temperature, the saturated liquid line has a positive slope and curvature, and the saturated vapor line has a negative slope and curvature. Incorrect changes are not observed along the isobars and isotherms.

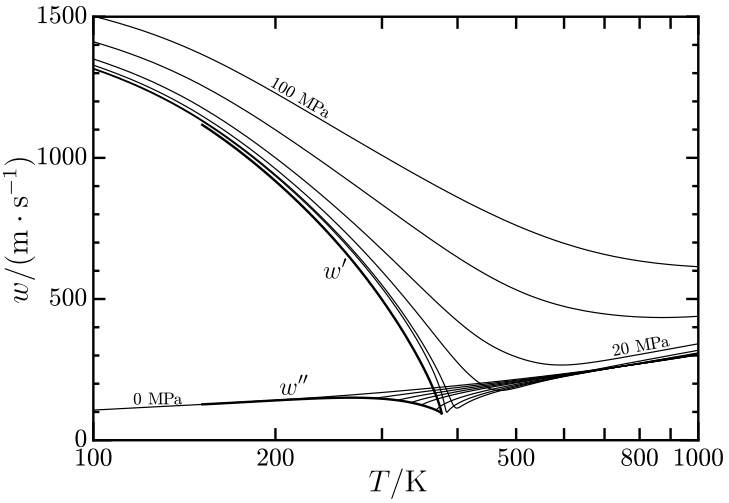

Fig. 17 Sound speed w versus temperature diagram. Isobars are shown at pressures of 0 MPa (ideal gas), 0.5 MPa, 1 MPa, 1.5 MPa, 2 MPa, 3 MPa, 4 MPa, 5 MPa, 10 MPa, 20 MPa, 50 MPa, 100 MPa, and the saturation boundaries.

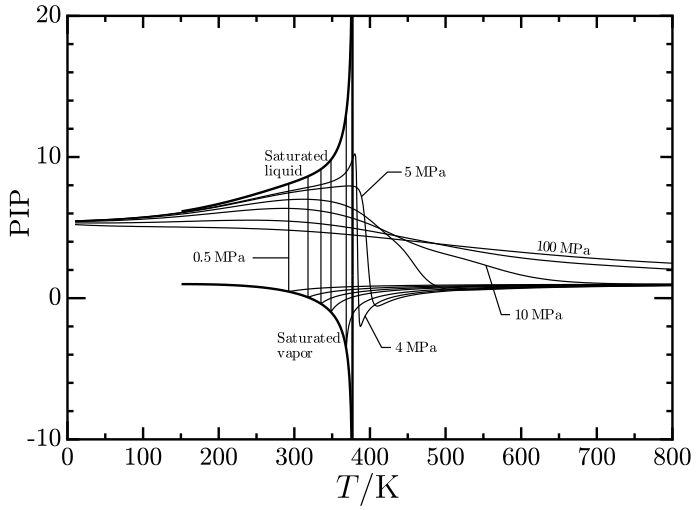

Fig. 18 Phase identification parameter (PIP) versus temperature diagram. Isobars are shown at pressures of 0.5 MPa, 1 MPa, 1.5 MPa, 2 MPa, 3 MPa, 4 MPa, 5 MPa, 10 MPa, 20 MPa, 50 MPa, 100 MPa, and the saturation boundaries.

7 ESTIMATED UNCERTAINTIES OF CALCULATED PROPERTIES

The equation of state developed in this work is valid from the triple point temperature (122.35 K) to 430 K at pressures up to 35 MPa. This equation is based

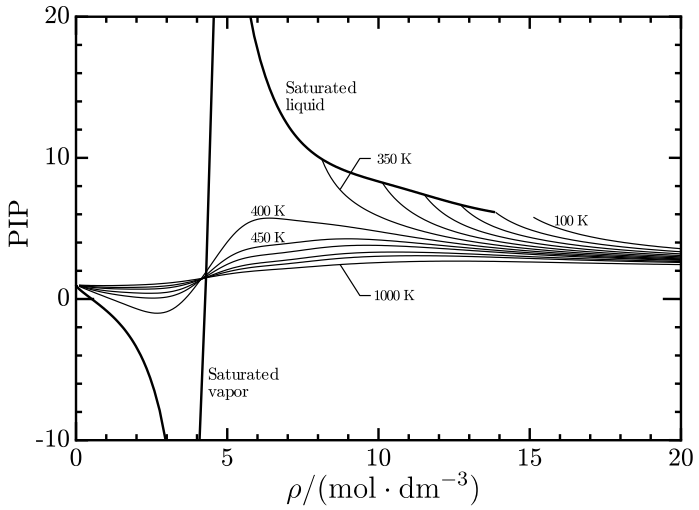

Fig. 19 Phase identification parameter (PIP) versus density diagram. Isotherms are shown at temperatures of 100 K, 150 K, 200 K, 250 K, 300 K, 350 K, 400 K, 450 K, 500 K, 600 K, 700 K, 1000 K, and the saturation boundaries.

on experimental data for the vapor pressure, (p, ρ, T) data including those at saturation, sound speeds in the vapor phase, isochoric heat capacities in the liquid phase, and ideal-gas isobaric heat capacity. The expected uncertainties ($k = 2$) in calculated properties are 0.1 % for vapor pressures, 0.1 % for liquid densities, 1 % for vapor densities, 0.3 % for saturated liquid densities, 1 % for saturated vapor densities, 0.06 % for vapor-phase sound speeds, and 2 % for liquid-phase isobaric heat capacities. These uncertainties are comprehensively based on the statistical analyses of deviations between reliable experimental data and calculated values from the equation of state. They are almost double the average deviations in experimental properties from calculated values. Various plots of constant-property lines demonstrate that not only does the equation exhibit correct behavior over all temperatures and pressures within the range of validity, but also that it shows reasonable extrapolation behav-

ior at extremely low and high temperatures, and at high pressures. Ancillary equations for vapor pressure and saturation densities have been developed that can be employed for fast approximate calculations of the saturation properties or as the initial values for iteration with the equation of state. We plan to further improve the equation if additional experimental data become available, such as liquid-phase sound speeds and (p, ρ, T) data at higher pressures.

As an aid in computer implementation, property values calculated from the equation of state are given in Table 6. Supporting Information provides a fluid file (R1243ZF.FLD) for use in REFPROP [48] and TREND [49].

Table 6 Calculated property values from the equation of state for R-1243zf to verify computer code.

T (K)	ρ ($\mathrm{mol \cdot dm^{-3}}$)	p (MPa)	c_v ($\mathrm{J \cdot mol^{-1} \cdot K^{-1}}$)	c_p ($\mathrm{J \cdot mol^{-1} \cdot K^{-1}}$)	w ($\mathrm{m \cdot s^{-1}}$)
280	0	0	76.6072	84.9217	163.915
280	11	7.393335	90.7467	130.734	648.467
280	0.1	0.2177605	79.7211	91.2493	155.465
360	8	3.992633	106.367	184.593	269.396
360	1	2.054891	103.218	146.368	135.631
378	4	3.582568	120.166	6522.37	93.0173

Appendix: Derivatives of the exponential terms in the residual Helmholtz energy

The derivatives of the exponential terms of Eq. 8 are given in the following equations:

$$\alpha^{\mathrm{r}}_{\mathrm{EXP}}(\tau,\delta) = \sum n_i \tau^{t_i} \delta^{d_i} \exp(-g_i \delta^{e_i}) \tag{15}$$

$$\delta \left(\frac{\partial \alpha^{\mathrm{r}}_{\mathrm{EXP}}}{\partial \delta} \right)_\tau = \sum n_i \tau^{t_i} \delta^{d_i} \exp(-g_i \delta^{e_i})(d_i - e_i g_i \delta^{e_i}) \tag{16}$$

$$\begin{aligned} \delta^2 \left(\frac{\partial^2 \alpha^{\mathrm{r}}_{\mathrm{EXP}}}{\partial \delta^2} \right)_\tau &= \sum n_i \tau^{t_i} \delta^{d_i} \exp(-g_i \delta^{e_i}) \\ &\quad \times \left[(d_i - e_i g_i \delta^{e_i})(d_i - 1 - e_i g_i \delta^{e_i}) - e_i^2 g_i \delta^{e_i} \right] \end{aligned} \tag{17}$$

$$\tau\delta \frac{\partial^2 \alpha^{\mathrm{r}}_{\mathrm{EXP}}}{\partial \tau \partial \delta} = \sum n_i \tau^{t_i} \delta^{d_i} \exp(-g_i \delta^{e_i}) \left[t_i (d_i - e_i g_i \delta^{e_i}) \right] \tag{18}$$

Acknowledgements The authors appreciate Aaron J. Rowane, National Institute of Standards and Technology, Boulder, and Hiroyuki Miyamoto, Toyama Prefectural University, for their assistance in documenting this paper.

Declarations

Competing interests

The authors declare that they have no conflict of interest.

Authors' contributions

RA contributed to evaluating available experimental data, fitting the consistent data to the final equation, and writing, reviewing, and editing the whole manuscript. EWL contributed to establishing the fitting techniques for reliable equations of state, coding a computer program to implement it, and reviewing the manuscript.

Funding

Partially funded by the National Institute of Standards and Technology

Availability of data and materials

Not applicable

References

1. S. González, E. Jiménez, B. Ballesteros, E. Martíinez, J. Albaladejo, Environ. Sci. Pollut. R. **22**, 4793 (2015). DOI 10.1007/s11356-014-3426-2
2. Z. Yang, X. Tang, J. Wu, J. Lu, Fluid Phase Equilib. **498**, 86 (2019). DOI 10.1016/j.fluid.2019.06.020
3. S. Li, S. Peng, Z. Yang, Y. Duan, Fluid Phase Equilib. **561**, 113542 (2022). DOI 10.1016/j.fluid.2022.113542
4. L. Fedele, G. Lombardo, D. Menegazzo, M. Scattolini, S. Bobbo, Int. J. Thermophys. **44**(6), 83 (2023). DOI 10.1007/s10765-023-03192-4
5. Z. Li, X. Wu, G. Hu, F. Tang, H. Guan, X. Zhu, J. Braz. Soc. Mech. Sci. Eng. **46**(8), 455 (2024). DOI 10.1007/s40430-024-04971-2
6. S. Peng, E. Wang, K. Qing, Z. Yang, Y. Duan, J. Chem. Thermodyn. **188**, 107164 (2024). DOI 10.1016/j.jct.2023.107164
7. G. Lombardo, D. Menegazzo, C. Wedler, L. Fedele, S. Bobbo, J. Trusler, Int. J. Thermophys. **45**(3), 34 (2024). DOI 10.1007/s10765-023-03321-z
8. R. Akasaka, Sci. Technol. Built Environ. **22**(8), 1136 (2016). DOI 10.1080/23744731.2016.1208000
9. R. Akasaka, E.W. Lemmon, J. Chem. Eng. Data **64**(11), 4679 (2019). DOI 10.1021/acs.jced.9b00007
10. M.J. Frisch, G.W. Trucks, H.B. Schlegel, G.E. Scuseria, M.A. Robb, J.R. Cheeseman, G. Scalmani, V. Barone, G.A. Petersson, H. Nakatsuji, X. Li, M. Caricato, A.V. Marenich, J. Bloino, B.G. Janesko, R. Gomperts, B. Mennucci, H.P. Hratchian, J.V. Ortiz, A.F. Izmaylov, J.L. Sonnenberg, D. Williams-Young, F. Ding, F. Lipparini, F. Egidi, J. Goings, B. Peng, A. Petrone, T. Henderson, D. Ranasinghe, V.G. Zakrzewski, J. Gao, N. Rega, G. Zheng, W. Liang, M. Hada, M. Ehara, K. Toyota, R. Fukuda, J. Hasegawa,

M. Ishida, T. Nakajima, Y. Honda, O. Kitao, H. Nakai, T. Vreven, K. Throssell, J.A. Montgomery, Jr., J.E. Peralta, F. Ogliaro, M.J. Bearpark, J.J. Heyd, E.N. Brothers, K.N. Kudin, V.N. Staroverov, T.A. Keith, R. Kobayashi, J. Normand, K. Raghavachari, A.P. Rendell, J.C. Burant, S.S. Iyengar, J. Tomasi, M. Cossi, J.M. Millam, M. Klene, C. Adamo, R. Cammi, J.W. Ochterski, R.L. Martin, K. Morokuma, O. Farkas, J.B. Foresman, D.J. Fox. Gaussian 09 Revision D.01 (2013). Gaussian Inc. Wallingford CT

11. Y. Higashi, N. Sakoda, J. Chem. Eng. Data **63**(10), 3818 (2018). DOI 10.1021/acs.jced.8b00452
12. Y. Higashi, N. Sakoda, M.A. Islam, Y. Takata, S. Koyama, R. Akasaka, J. Chem. Eng. Data **63**(2), 417 (2018). DOI 10.1021/acs.jced.7b00818
13. G. Di Nicola, C. Brandoni, C.D. Nicola, G. Giuliani, J. Therm. Anal. Calorim. **108**(2), 627 (2012). DOI 10.1007/s10973-011-1944-4
14. S. Tomassetti, G. Di Nicola, C. Kondou, Int. J. Refrig. **133**, 172 (2022). DOI 10.1016/j.ijrefrig.2021.10.008
15. M.E. Wieser, M. Berglund, Pure Appl. Chem. **81**(11), 2131 (2009). DOI doi:10.1351/PAC-REP-09-08-03
16. E. Tiesinga, P.J. Mohr, D.B. Newell, B.N. Taylor, J. Phys. Chem. Ref. Data **50**(3), 033105 (2021). DOI 10.1063/5.0064853
17. E.W. Lemmon, A.R.H. Goodwin, J. Phys. Chem. Ref. Data **29**(1), 1 (2000). DOI 10.1063/1.556054
18. K. Gao, J. Wu, P. Zhang, E.W. Lemmon, J. Chem. Eng. Data **61**(8), 2859 (2016). DOI 10.1021/acs.jced.6b00195
19. R. Span, *Multiparameter Equations of State: An Accurate Source of Thermodynamic Property Data* (Springer Berlin, 2000)
20. E.W. Lemmon, M.O. McLinden, W. Wagner, J. Chem. Eng. Data **54**(12), 3141 (2009). DOI 10.1063/1.556054
21. H.J. Kretzschmar, T. Zschunke, J. Klinger, A.I. Dittman, *An Alternative Method for the Numerical Calculation of the Maxwell Criterion in Vapour Pressure Computations, Properties of Water And Steam: Proceedings of The 11th International Conference* (CRC Press, 1990)

22. R. Akasaka, J. Therm. Sci. Technol. **3**(3), 442 (2008). DOI 10.1299/jtst.3.442

23. D.A. McQuarrie, *Statistical Mechanics, Chapter 8* (Harper & Row, 1975)

24. H. Chen, K. Zhang, Z. Yang, Y. Duan, J. Chem. Eng. Data **66**(5), 2256 (2021). DOI 10.1021/acs.jced.1c00098

25. R. Akasaka, Y. Zhou, E.W. Lemmon, J. Phys. Chem. Ref. Data **44**(5), 013104 (2015). DOI 10.1063/1.4913493

26. R. Akasaka, Y. Higashi, N. Sakoda, S. Fukuda, E.W. Lemmon, Int. J. Refrig. **119**(11), 457 (2020). DOI 10.1016/j.ijrefrig.2020.07.011

27. R. Akasaka, E.W. Lemmon, J. Phys. Chem. Ref. Data **51**(2), 023101 (2022). DOI 10.1063/5.0083026

28. E.W. Lemmon, R. Akasaka, Int. J. Thermophys. **43**(8), 119 (2022). DOI 10.1007/s10765-022-03015-y

29. E.W. Lemmon, R.T. Jacobsen, J. Phys. Chem. Ref. Data **34**(1), 69 (2005). DOI 10.1063/1.1797813

30. S. Herrig, M. Thol, A.H. Harvey, E.W. Lemmon, J. Phys. Chem. Ref. Data **47**(5), 043102 (2018). DOI 10.1063/1.5053993

31. M. Thol, E.W. Lemmon, R. Span, High Temp.-High Press. **41**(2), 81 (2012)

32. R. Akasaka, E.W. Lemmon, Int. J. Thermophys. **44**(11), 166 (2023). DOI 10.1007/s10765-023-03266-3

33. R. Romeo, E.W. Lemmon, Int. J. Thermophys. **43**(10), 146 (2022). DOI 10.1007/s10765-022-03059-0

34. T.E. Daubert, J.W. Jalowka, V. Goren, AIChE Symposium Series **256**(1), 128 (1987). DOI 10.1007/s10765-013-1553-5

35. J.S. Brown, G.D. Nicola, L. Fedele, S. Bobbo, C. Zilio, Fluid Phase Equilib. **351**(8), 48 (2013). DOI 10.1016/j.fluid.2012.09.036

36. J. Yin, J. Ke, G. Zhao, S. Ma, Int. J. Refrig. **117**, 175 (2020). DOI 10.1016/j.ijrefrig.2020.04.021

37. G. Di Nicola, J.S. Brown, L. Fedele, M. Securo, S. Bobbo, C. Zilio, Int. J. Refrig. **36**(8), 2209 (2013). DOI 10.1016/j.ijrefrig.2013.08.004

38. L. Ding, B. Sheng, Y. Hou, X. Dong, Y. Zhao, H. Xu, J. Shen, M. Gong, J. Chem. Thermodyn. **161**, 106494 (2021). DOI 10.1016/j.jct.2021.106494

39. L.D. Tenardi, O. Frotscher, X. Yang, F. Jiao, M. Richter, P.L. Stanwix, E.F. May, Int. J. Thermophys. **44**(1), 14 (2023). DOI 10.1007/s10765-022-03120-y

40. B. Sheng, Z. Li, W. Liu, X. Chen, Y. Zhao, X. Dong, H. Yan, J. Shen, M. Gong, J. Chem. Thermodyn. **153**, 106319 (2021). DOI 10.1016/j.jct.2020.106319

41. B. Sheng, Y. Zhao, X. Dong, E. Luo, M. Gong, J. Chem. Thermodyn. **194**, 107277 (2024). DOI 10.1016/j.jct.2024.107277

42. G. Raabe, J. Chem. Eng. Data **65**(3), 1234 (2020). DOI 10.1021/acs.jced.9b00588

43. K.A. Gillis, M.R. Moldover, Int. J. Thermophys. **17**, 1305 (1996). DOI 10.1007/BF01438672

44. M. Thol, G. Rutkai, A. Köster, R. Lustig, R. Span, J. Vrabec, J. Phys. Chem. Ref. Data **45**(2) (2016). DOI 10.1063/1.4945000

45. M. Thol, F. Fenkl, E.W. Lemmon, Int. J. Thermophys. **43**, 41 (2022). DOI 10.1007/s10765-021-02961-3

46. F. Fiedler, J. Karog, E.W. Lemmon, M. Thol, Int. J. Thermophys. **44**(10), 153 (2023). DOI 10.1007/s10765-023-03258-3

47. G. Venkatarathnam, L.R. Oellrich, Fluid Phase Equilib. **301**(4), 225 (2011). DOI 10.1016/j.fluid.2010.12.001

48. E.W. Lemmon, I.H. Bell, M.L. Huber, M.O. McLinden. NIST Standard Reference Database 23: Reference Fluid Thermodynamic and Transport Properties-REFPROP, Version 10.0, National Institute of Standards and Technology (2018). DOI 10.18434/T4JS3C. URL `https://www.nist.gov/srd/refprop`

49. R. Span, R. Beckmüller, S. Hielscher, A. Jäger, E. Mickoleit, T. Neumann, S. Pohl. TREND. Thermodynamic Reference and Engineering Data 5.0. Lehrstuhl für Thermodynamik, Ruhr-Universität Bochum. (2020). URL `https://www.thermo.ruhr-uni-bochum.de/thermo/forschung/zustandsgleichung_trend.html.de`